Recrystallisation behaviour of a fully austenitic Nb-stabilised stainless steel

DOI:
10.1111/jmi.12776

Document Version
Accepted author manuscript

Recrystallisation behaviour of a fully austenitic Nb-stabilised stainless steel

Journal:	*Journal of Microscopy*
Manuscript ID	JMI-2018-0121.R1
Wiley - Manuscript type:	Original Article
Date Submitted by the Author:	19-Nov-2018

Complete List of Authors:	Barcellini, Chiara; University of Manchester Dumbill, Simon; National Nuclear Laboratory Ltd Jimenez-Melero, Enrique; University of Manchester

Keywords:	scanning electron microscopy, Austenitic stainless steel, advanced gas reactor, recrystallisation, niobium carbo-nitrides

Recrystallisation behaviour of a fully austenitic Nb-stabilised stainless steel

Chiara Barcellini[a,*], Simon Dumbill[b], Enrique Jimenez-Melero[a]

[a]*Materials Performance Centre, School of Materials, The University of Manchester, Manchester M13 9PL, UK*

[b]*National Nuclear Laboratory, Sellafield, Seascale CA20 1PG, United Kingdom*

*Corresponding author

Email: chiara.barcellini@postgrad.manchester.ac.uk

University of Manchester

School of Materials

Materials Performance Centre

Oxford Road

Manchester

M13 9PL

United Kingdom

Summary:

We have performed an in-depth characterisation of the microstructure evolution of 20Cr-25Ni Nb-stabilised austenitic stainless steel during 1h isochronal annealing up to 1100°C using scanning electron microscopy. This steel grade is used as cladding material in advanced gas-cooled fission reactors, due to its resistance to thermal creep and oxidation. The initial deformed microstructure undergoes recrystallisation via a strain-induced boundary migration mechanism, attaining a fully recrystallised microstructure at 850°C. A number of twins are observed in the vicinity of deformation bands prior to the start of recrystallisation. New Nb(C,N) particles form gradually in the microstructure, and the particle dispersion presents a maximum volume fraction of 2.7% at 930°C. At higher temperatures, the smaller particles become unstable and gradually dissolve in the matrix. Consequently, the Zener pinning pressure exerted on the grain boundaries is progressively released, triggering the growth of the austenite grains up to an average size of ~47μm at 1100°C. The observed temperature window for recrystallisation and grain growth can be predicted by a unified model based primarily on the migration of high and low angle grain boundaries.

Lay Description:

Austenitic stainless steel containing high percentage of chromium and nickel is currently used as fuel cladding material in the British Advanced Gas-cooled Reactors (AGR). This material has been chosen because of its high resistance to thermal creep and corrosion, both enhanced by the presence of a fine dispersion of carbo-nitrides precipitated during the cladding thermomechanical processing. During the time spent in the reactor core, few fuel cladding elements can become susceptible to local chromium depletion at grain boundaries, which is ascribed to the time evolution of the microstructural damage caused by the neutron bombardment in the reactor core. This depletion might increase the susceptibility of this steel to intergranular corrosion attacks during medium-to-long term storage of spent fuel elements in water ponds. The severity of the local chromium depletion depends not only on the irradiation conditions, but also on the grain boundary geometry. We have investigated the recovery, recrystallisation and grain growth of AGR stainless steel during 1h annealing at selected temperatures relevant for the thermomechanical processing of the steel claddings, focusing on the formation and evolution of grain boundaries and second phases. These two features play a key role in the progression of the neutron damage and the subsequent development of local chromium depletion during reactor service operations. A deep understanding of the mechanisms and conditions behind their formation during the thermomechanical processing of the cladding material and their interaction with each other constitutes the foundation to evaluate, and potentially mitigate, the effect of irradiation on the cladding material.

Keywords: Austenitic stainless steel, advanced gas reactor, recrystallisation, niobium carbo-nitrides, scanning electron microscopy.

1. Introduction

Nb-stabilised stainless steel containing 20wt.%Cr and 25wt.%Ni is a dispersion-hardened alloy with a face-centered-cubic (fcc) austenitic matrix, used as cladding material for the slightly enriched (up to 3.5% U-235) uranium dioxide-based fuel in UK Advanced Gas-cooled fission Reactors (AGRs). The relatively high amount of Cr and Ni in this steel grade is aimed at increasing the material's resistance to oxidation [Lobb, R. C., Evans, H.E. (1984)] and at stabilising the austenite phase in the temperature range of the reactor core, i.e. 350-700°C [Taylor, C. (1986)], respectively. Moreover, the formation of Nb carbo-nitrides prior to the cladding lifetime in the reactor is meant to control the austenite grain size, increase the material's resistance to thermal creep in the oxidising AGR core environment [Knowles, G. (1977)], and also trap carbon and nitrogen so as to prevent the formation of chromium-containing carbides and nitrides at the grain boundaries of the matrix [Ramaswamy, V., West, D. R. F (1970) , Sourmail, T. (2001)]. The discharged fuel and the cladding are planned to be stored upon removal from the reactor core in caustic-dosed water ponds for at least 25 years [Whillock, G. O. H., Hands, B. J., Majchrowski, T. P., Hambley, D. I. (2018)]. A reduction in the local Cr content below 12wt.% would increase the susceptibility of this steel to intergranular corrosion attacks during medium-to-long term storage in aqueous environments [Whillock, G. O. H., Hands, B. J., Majchrowski, T. P., Hambley, D. I. (2018), Al-Shater, A., Engelberg, D., Lyon, S., Donohoe, C.,Walters, S., Whillock, G., Sherry, A. (2017)].

Despite the formation of Nb(C, N) particles during the steel processing, yielding a reduction in free interstitials in the matrix available to bind with Cr under reactor service conditions, significant Cr depletions have been detected in specific fuel cladding pins (i) at the (sub-)surface due to the C intake from the CO_2-based coolant leading to the formation of Cr carbides, and (ii) through the cladding wall thickness triggered by the evolution in time of the microstructural damage caused by the neutron bombardment in the reactor core [Taylor, C. (1986)]. As a consequence of the latter process, the steel cladding can become susceptible to intergranular corrosion attacks and stress corrosion cracking in storage water ponds containing a concentration of ≥ 0.2 mg/L Cl^- [Whillock, G. O. H., Hands, B. J., Majchrowski, T. P., Hambley, D. I. (2018)]. This phenomenon, termed radiation-induced sensitisation [Kenik, E. A., Inazumi, T., Bell, G. E. C. (1991)], is understood to be a consequence of the evolution of self-interstitials and vacancies after the heat spike of the radiation-induced displacement cascade, together with the coupling of point defect diffusion with a biased flux of Cr atoms away from grain boundaries, and concomitantly of Ni, Si and P towards grain boundaries [Was., G. (2007), Ardell, A. J. , Bellon, P. (2016)]. Radiation-induced solute redistribution and the consequent sensitisation affects the AGR fuel cladding pins that operate at 350-520°C, with a peak effect at ~420°C [Taylor, C. (1986)]. Recent work on 304 stainless steel revealed that a high-density twin network can inhibit the Cr depletion and carbide formation at grain boundaries, consequently yielding a higher corrosion potential, a wider passivation range and a lower corrosion rate [Chen, A. Y. *et al*. (2017)].

An in-depth understanding of the mechanisms and conditions behind the formation of grain boundaries (GB) during the thermomechanical processing of the cladding material and the GB interaction with the fine Nb(C,N) particle dispersion, constitutes the foundation to evaluate, and potentially mitigate, the effect of irradiation on the AGR cladding material. In this study, we have investigated the recovery, recrystallisation and grain growth of AGR stainless steel during 1h annealing at selected temperatures up to 1100°C. We have monitored the evolution of the grain boundaries and the second phase particles, both of which play a key role during the in-reactor lifetime of the AGR claddings. Numerous models for recovery [Nes, E. (1995), Huang, Y., Humphreys, F. J. (2000)], recrystallization [Johnson, W. A., Mehl, R. F. (1939), Avrami, M. (1939), Avrami, M. (1940), Avrami, M. (1941), Kolmogorov, A. N. (1937), Fanfoni, M., Tomellini, M. (1998), Burke, D. T. J. (1952)] and grain growth [Burke, D. T. J. (1952), Smith. C. S. (1948), Andersen, I., Grong, Ø., Ryum, N. (1995b)] have been proposed for metallic materials throughout the years. However, they are often applied to high purity metals or model alloys, where the effects of single parameters can be isolated unequivocally. In this study, we have used the unified model proposed by Humphreys [Humphreys, F. J. (1997a), Humphreys, F.J. (1997b)] to evaluate the observed annealing behaviour of 20Cr-25Ni Nb-stabilised stainless steel.

2. Experimental

The as-received material, whose composition is reported in Table 1, was in the form of a 100×50 mm^2 plate with a thickness of 0.5mm and had been produced to meet the current cladding requirements for UK AGRs. Additional information regarding the production route of AGR claddings is reported in [Al-Shater, A., Engelberg, D., Lyon, S., Donohoe, C.,Walters, S., Whillock, G., Sherry, A. (2017), Powell, D. J., Pilkington, R., Miller, D. A. (1985), Barcellini, C. Dumbill, S. Jimenez-Melero E. (2018)] In this work, samples with dimensions of 5×5 mm^2 were cut and heat treated for 1h at selected temperatures up to 1100°C in inert atmosphere, and subsequently water quenched to room temperature. Afterwards, those samples were mechanically ground and polished with a 0.25 µm colloidal silica suspension. Vickers hardness measurements were taken using a load of 1kg. The hardness value reported for each sample corresponds to the mean value of ten indentations. Chemical etching with an oxalic acid 10 vol.% solution was performed at 6V for 25-30s prior to optical microscopy, in order to reveal the grain boundaries of the austenitic matrix. The average austenite grain size was calculated using the linear intercept method from optical micrographs. The average value for each sample was derived using ten measurements excluding twin boundaries.

An FEI Magellan HR FEG-SEM (resolution of ~2nm using an accelerating voltage of 5kV and a beam current of 0.8nA [Young, R., Henstra, S., Chmelik, J., Dingle, T., Mangnus, A., Van Veen, G., Gestmann, I. (2009), Roussel, L. Y., Stokes, D. J., Gestmann, I., Darus, M., Young, R. J. (2009)]) equipped with both a concentric backscattered (CBS) detector and an electron backscattered diffraction (EBSD) detector was used to collect high-resolution back-scattered electron (BSE) micrographs and EBSD maps covering a total area of 145×65μm^2 with a step size of 0.15μm. The EBSD data processing was performed using the MTEX software [Bachmann, F., Hielscher, R., Schaeben, H. (2010)]. The derived EBSD maps were used to analyze the grain boundary characteristics and their evolution with temperature. The observed grain boundaries were classified into low-angle grain boundaries (LAGB) presenting a misorientation angle between 2 and 15° [Humphreys, F. J. (2001), Humphreys, F. J. (1999)], coincidence site lattice boundaries (CSL) [Kronberg, M. L., Wilson, F. H. (1949), Randle, V., Brown, A. (1989)] and high-angle grain boundaries (HAGB). A high-angle grain boundary was classified as a CSL boundary of the type Σ3, Σ5, Σ9 or Σ11 when Brandon's criterion was satisfied [Brandon, D. G. (1996)]. Other types of CSL boundaries were not considered in this study, since they were not observed in significant numbers. The length fraction of a given type of GB was calculated as the ratio between the length of that type of boundary and the total length of grain boundaries observed in the EBSD map of a given sample. The EBSD data were also used to obtain the recrystallisation fraction (f_{RX}) as a function of annealing temperature and the average sub-grain dimension. The first was calculated as the change in HAGB length fraction, including CSL boundaries, according to the expression [Jazaeri, H., Humphreys, F. J. (2004)]:

$$f_{RX} = \frac{HAGB_T - HAGB_D}{HAGB_R - HAGB_D} \quad (1)$$

where $\mathrm{HAGB_D}$ corresponds to the length fraction of HAGB prior to recrystallisation, $\mathrm{HAGB_R}$ after complete recrystallisation, and $\mathrm{HAGB_T}$ at a temperature *T*. The latter was obtained using the linear intercept method from EBSD maps considering only interception with LAGB [Humphreys, F. J. (2001)]. After grain reconstruction, the orientation distribution function was derived using the Bunge convention for the three Euler angles [30], and thereupon inverse pole figure colour maps were obtained.

Furthermore, the average diameter of the Nb(C,N) particles was measured using the BSE micrographs, and their volume fraction (f_v) was estimated as the area occupied by the particles over the total area of the micrograph [Humphreys, F. J., Hatherly, M. (2012)]. Five BSE micrographs, each covering an area of ~138μm^2, were used for each specimen in order to estimate the volume fraction, average diameter and the standard deviation of the measurements. A FEI Tecnai G2 20 TEM microscope equipped with a Gatan CCD camera was used to assess the presence of nanometric carbide particles in the microstructure, whereas a FEI Talos F200A TEM/STEM microscope was used to investigate the chemistry of those second phase particles.

3. Results

3.1. Matrix evolution during isochronal annealing

Fig. 1 shows the evolution of the microstructure of 20Cr-25Ni Nb-stabilized stainless steel after annealing for 1h at selected temperatures. The material has been received in a deformed condition, which resembles the microstructure reported for an equivalent steel grade that had undergone 25% cold work at room temperature [Jones, A. R., Howell, P. R., Ralph, B. (1977)]. Elongated sub-grains (see Fig 2a), shear bands (see Fig 1a and b) and deformation twins (see Fig 2a) characteristic of cold worked austenitic stainless steel are still visible at 400°C and 600°C. Fig. 2a and b display illustrative examples of inverse pole figures and grain boundary misorientation maps, respectively, of the same region of interest for each selected temperature, whereas the change in the average micro-hardness and austenite grain size with temperature is shown in Fig. 3, together with the evolution of the GB length fraction. The principal parameters that characterise the annealing behavior of this steel at the studied temperatures are collected in Table 2. Even though no recrystallised grains are observed in the microstructure up to 600°C, the increase in the average GB misorientation from ~15° in the as-received condition to ~23° at 600°C suggests that rearrangements of the GB dislocations are already taking place at that temperature. Between the as-received condition and 600°C the LAGB fraction decreases while the length fraction of CSL boundaries, especially Σ3, increases by approx. four times. The new twins are formed mainly at deformation bands, as illustrated in Fig. 2b for the annealing temperature of 600°C. This GB rearrangement of the boundaries does not cause a significant change in the average hardness value of the material, see Fig. 3a.

Small recrystallised grains are observed at 700°C at the edge of shear bands (Fig. 1c), together with a significant softening of the material. The mean GB misorientation increases to ~29° at this annealing temperature, and the increase in the length fraction of CSL boundaries is higher than that of HAGB. The estimated recrystallisation fraction is 36%. In Fig. 1d a recrystallisation front consuming a deformed region of the microstructure can be observed at 800°C. At this temperature, the recrystallisation fraction amounts to 89%. The fraction of HAGB and CSL is similar, i.e. ~45% for each of them. At 850°C, the recrystallisation process is completed and the average austenite grain size is ~3.8μm. Between 850°C and 950°C, the austenitic matrix does not change significantly, with a grain size of ~4μm and only minor changes in the GB characteristics. Beyond 950°C, the austenite grains adopt a polygonal shape and their average size increases up to a value of ~47μm at 1100°C, together with a gradual reduction in sample hardness.

3.2. Second phase particles

The presence of second phase particles in the microstructure during annealing can be observed in Fig 2c, the temperature dependence of the average particle diameter and volume fraction is shown in Fig 3c. The chemical composition of the second phase particles detected was determined with STEM/EDX microanalysis. They have been found to be enriched in Nb, and have been identified as Nb(C,N). Only after 1h of annealing at 930°C, clear signs of Ni and Si enrichment were observed in those particles with a diameter larger than ~50nm [Barcellini, C., Dumbill, S., Jimenez-Melero E. (2018)].

A particle distribution with an average diameter of 161nm was already present in the as-received material. We have observed an overall decreasing trend in the average particle diameter with increasing temperature up to 930°C, and concomitantly an increase in the particle volume fraction, in the temperature region where recrystallisation takes place in the austenitic matrix. The maximum volume fraction was observed at 930°C and amounted to 2.66%. These observations indicate the formation of new smaller carbides with increasing temperature up to 930°C. The particle distribution is not homogeneous and they tend to be located close to grain boundaries, as can be observed in the BSE image of the microstructure at 930°C, see Fig. 2c. In contrast, the opposite trend occurs in the region between 930°C at 1100°C, where the particles become bigger progressively, reaching an average diameter of 156nm that lies very close to its value in the as received condition. The trend in the particle volume fraction is also reverted, falling rapidly down to ~0.09 % at 1100°C. These facts reveal that the smaller Nb(C,N) particles are not stable above 930°C and dissolve gradually with increasing temperature.

4. Discussion

20Cr-25Ni Nb-stabilized steel can be modelled as a two-phase alloy. The predominant phase is fcc austenite, whereas the dispersion of Nb(C,N) particles constitutes the second or minority phase. Those two phases evolve together in the temperature range investigated in this study. We have used the unified model proposed by Humphreys [Humphreys, F. J. (1997a), Humphreys, F. J. (1997b)], according to which the evolution of a given cellular microstructure during annealing occurs primarily by the migration of high and low angle grain boundaries. The austenite matrix can be described as an assembly of equiaxed grains or subgrains, characterized by an average radius $\overline{R}$ and a set of average grain boundary properties, namely the misorientation $\overline{\theta}$, mobility $\overline{M}$ and energy $\overline{\gamma}$. We can then consider the behavior of a particular austenite grain or subgrain R with boundary properties (θ, M, γ). The spherical Nb(C,N) particle dispersion can be characterized at varying annealing temperatures by its volume fraction f_v and its average particle diameter d. Those Nb(C,N) particles exert an average Zener pinning pressure $\overline{P}_z$ on the migrating austenite boundary of energy γ [Nes, E., Ryum, N., Hunderi, O. (1979), Humphreys, F.J. (1979)]. The condition for the instability leading to abnormal or discontinuous grain growth of a particular austenite grain of radius R is expressed by the following inequality [Humphreys, F. J. (1997a), Thompson, C. V., Frost, H. J., Spaepen, F. (1987)]:

$$\bar{R}\frac{dR}{dt} - R\frac{d\bar{R}}{dt} > 0 \quad (3)$$

where t represents the annealing time. This expression can be re-written using microstructural parameters as follows:

$$\bar{R}M\left(\frac{\bar{\gamma}}{R} - \frac{\gamma}{R} - \frac{Z\gamma}{\bar{R}}\right) - \frac{R\bar{M}}{\bar{R}}\bar{\gamma}\left(\frac{1}{4} - Z\right) > 0 \quad (4)$$

where Z is a dimensionless parameter which contains in this case the properties of the Nb(C,N) dispersion, according to:

$$Z = \frac{\bar{R}}{\bar{\gamma}}\overline{P_z} = \frac{3f_v\bar{R}}{d} \quad (5)$$

The Z values as a function of annealing temperature are given in Table 2. The austenite grain boundary mobility, M, and energy, γ, can both be expressed as a function of the boundary misorientation θ, whose value can be derived from the collected EBSD maps. The mobility can be expressed as a sigmoidal dependence on the boundary misorientation, according to [Humphreys, F. J., Hatherly, M. (2012), Gottstein, G., Shvindlerman, L. S. (1992),]:

$$M = M_m\left[1 - e^{-B\left(\frac{\theta}{\theta_m}\right)^n}\right] \quad (6)$$

whereas the boundary energy adopts the Read-Shockley relationship [38]:

$$\gamma = \gamma_m\frac{\theta}{\theta_m}\left(1 - ln\frac{\theta}{\theta_m}\right) \quad (7)$$

The constants M_m, θ_m and γ_m represent the mobility, misorientation and energy of a HAGB, whereas the parameters n and B take the values 4 and 5, respectively [Humphreys, F.J. (1997b)]. Eq. 4 can be solved for the different annealing phenomena, such as recovery, recrystallisation and grain growth, and can be used to predict which of those mechanisms dominates for a given assembly of grains or subgrains and a selected annealing temperature.

We have applied this model to the observed annealing behavior of 20Cr-25Ni Nb-stabilized steel, using as input the experimental data contained in the blue (recovery), green (recrystallisation) and red (grain growth) regions of Fig. 3. The solutions of Eq. 4 are shown in Fig. 4a for recovery and recrystallisation, and in 4b in the case of grain growth. The black curves in Fig. 4a have been obtained assuming that the maximum austenite grain diameter is 2.5 times the average grain diameter of the particle size distribution. This hypothesis relies on the fact that the austenite matrix is characterized by a log-normal size distribution, and only very few grains do not satisfy the aforementioned hypothesis. The blue curve has, by contrast, been obtained by removing this hypothesis and allowing grains of any size (R=∞) [Humphreys, F. J. (1997a), Humphreys, F. J. (1997b)]. In Fig. 4b, the minimum and maximum values of the austenite radius ratio $R/\overline{R}$ for abnormal grain growth are show as a function of the Z parameter. All the $R/\overline{R}$ values between those two limits are solutions of Eq. 4. The maximum size ratio which can be achieved by abnormal growth is less than 5 if Z<0.1. Below that Z value a broadening of the grain size distribution is predicted to occur, instead of abnormal grain growth, and normal grain growth for the limit case of Z = 0 [Humphreys, F.J. (1997b)].

Fig. 4a represents the Z-$\overline{\theta}$map that predicts under what conditions either discontinuous subgrain growth or recrystallisation is expected to occur, together with the data points for selected annealing temperatures ≤800°C. The boundary between both processes depends on the misorientation angle θ. The as-received microstructure consists of an assembly of subgrains with a mean diameter of 1.2µm and mean boundary misorientation of 5.3°. Recrystallisation for such an assembly is inhibited in the case of $Z \geq 0.72$ [Humphreys, F.J. (1997b)]. Since Z is 0.072, we would expect to observe upon heating evidence of recrystallised grains. However, no obvious indication of recrystallisation has been detected after 1h annealing at either 400°C ($Z=0.016\pm0.009$) or 600°C ($Z=0.035\pm0.024$). The lack of clear signs of recrystallisation in the blue region of Fig 3 might be due to a combination of low temperatures and a relatively short annealing time. In the as-received material and in the specimens heat treated at 400°C and 600°C, more than 60% of the boundaries observed in the austenitic matrix are LAGB, whose mobility is a function of the misorientation angle and of the temperature [Sutton, A. P., Balluffi. R. W. (1996), Gottstein, G., Shvindlerman, L. S. (1992)]. The activation energy of LAGB migration is significantly higher than that of HAGB [Humphreys, F. J., Hatherly, M. (2012)]. Alternatively, the microstructure could undergo a recovery process termed discontinuous subgrain growth [Vandermeer, R. A. (1995)]. At 600°C the average misorientation of the subgrain structure decreases to 4.5°, therefore the Z value inhibiting recrystallisation reduces to $Z \geq 0.66$. Since Z is only 0.035, one can expect that such a microstructure lowers its internal energy instead via recrystallisation. However, annealing the as-received microstructure up to 600°C induced instead a rearrangement of the grain boundary dislocations, and the formation of a significant number of twins in the regions of maximum local strains such as deformation bands. Twins are understood to form in deformed fcc metals by lateral growth of very thin deformation twins in the early stage of annealing, and they might form every time the free energy of a certain boundary and its twin is less than that of the boundary and its neighbors [Carpenter, H. C. H., Tamura, S. (1962),] Fullman, R. L., Fisher, J.C. (1951)]. The discontinuities in mobility [Sutton, A. P., Balluffi. R. W. (1996),] and energy [Rohrer, G. S. (2011)] of twin and special CSL boundaries are not fully-described in this model, which considers those quantities to be a continuous function of the misorientation angle [Humphreys, F. J. (1997a), Humphreys, F. J. (1997b)]. Special boundaries are known to have a lower activation energy for migration than LAGB and randomly-oriented HAGB [Gottstein, G., Shvindlerman, L. S. (1992)], and their activation energy is not highly affected by impurities [Fridman, E. M., Kopetskji, C. V., Shvindlerman, L. S. (1975), Gottstein, G., Shvindlerman, L. S. (1992)].

For temperatures lower than 700°C (blue region of Fig. 3) no precipitation of additional Nb(C,N) particles was observed, probably due to the relatively short annealing time used in this study. According to the time-temperature-precipitation diagram of Powell and co-workers, the optimum temperature for Nb carbo-nitrides lies between 650 and 700°C for longer annealing times (>10^2h) [Powell, D. J., Pilkington, R., Miller, D. A. (1988)]. The precipitation kinetics and nucleation sites of Nb(C,N) particles in Nb-stabilised austenitic stainless steel depend on the recrystallisation fraction and on the supersaturation of C and N in the matrix prior annealing. However at least 10h of annealing at 650°C are needed to precipitate significant amounts of nano-sized Nb(C,N) [Dewey, M. P. A., Sumner, G., Brammar, I. S. (1965)]. This is in agreement with our EM observations at temperatures ≤600°C within the experimental uncertainty of the measurements. According to the reported TTP diagram, temperatures ≥750°C are required in order to precipitate this second phase during shorter heat treatments, [Powell, D. J., Pilkington, R., Miller, D. A. (1988)]. Moreover, pre-existing Nb(C,N) particles are expected to be stable in this low-temperature range for short annealing times [Vujic, S., Sandstrom, R., Sommitsch, C. (2015)].

The green region in Fig. 3 is the one in which recrystallisation takes place to full completion, attaining a microstructure that contains a relatively large number of HAGB and CSL boundaries and a fine dispersion of Nb(C,N) particles. The data points in Fig. 4a for 700°C and 800°C fall in the region in the Z-$\overline{\theta}$map where discontinuous subgrain growth is predicted by the model if $R = 2.5\overline{R}$ is supposed. This process has rarely been observed experimentally [Huang, Y., Humphreys, F. J. (2000)], because its occurrence critically depends on the misorientation of a particular subgrain relative to the subgrain assembly mean misorientation [Humphreys, F.J. (1997b)]. Only those subgrains with a misorientation θ between ~$0.7\overline{\theta}$ and $1.5\overline{\theta}$ are likely to undergo this process [Humphreys, F.J. (1997b)]. In the case of the specimen heat treated at 700°C the probability that a subgrain has a misorientation in that range is $2 \cdot 10^{-1}$, whereas at 800°C the probability decreases to $5 \cdot 10^{-2}$. The model used predicts a wider range of conditions for discontinuous subgrain growth to occur also because of the hypothesis on the maximum subgrain size ($R = 2.5\overline{R}$). If we do not impose it and suppose that subgrains of larger size may exist in the microstructure (R= ∞), the specimens heat treated at either 700 or 800°C fall in the region in the Z-$\overline{\theta}$map where recrystallisation is predicted (see the blue curve in Fig. 5a). Our experimental data reveals clear signs of recrystallisation at 700 and 800°C, see Fig. 1c and 1d. Once the microstructure is fully recrystallised at 850°C, it does not change significantly until 950°C. Recrystallisation originates in regions in the microstructure characterized by a high misorientation gradient such as deformation bands [Huang, Y., Humphreys, F. J. (2000)], where either sufficient large subgrains close to pre-existing HAGBs are already present after plastic deformation [Huang, Y., Humphreys, F. J. (2000)], or can form through the transition from LAGB into HAGB structure during the early stages of annealing via the re-arrangement of extrinsic GB dislocations [Fullman, R. L., Fisher, J.C. (1951)]. Recrystallisation then proceeds through strain induced boundary migration (SIBM), where the mobile HAGBs migrate to regions of higher stored energy, i.e. higher local misorientation [Lobb, R. C., Evans, H.E. (1984)], leaving a region behind with a relatively low dislocation density [Huang, Y., Humphreys, F. J. (2000)]. Fig. 5 shows an illustrative example of small recrystallised grains formed close to a deformation band, where the bulging boundaries of the recrystallisation front which surround the non-recrystallised deformation band are clearly visible.

During the recrystallisation of the austenite matrix, there is also a steady increase in the volume fraction of the second phase particles, which reaches its maximum at 930°C, coupled with an overall trend of decreasing particle size. Once the recrystallisation is completed, carbides are often found at HAGB and CSL boundaries of the matrix, see Fig. 6, hindering the migration of GBs and therefore delaying grain growth. The microstructure at 930°C is characterized by a mean grain misorientation of θ~49° and a Z value of ~1.9. Eq.4 predicts that grain growth is inhibited for $Z \geq 1$. Our previous investigation of the microstructural evolution at 930°C as a function of annealing time showed that the grain boundary migration destabilises a number of small Nb(C,N) particles, which dissolve and subsequently re-precipitate at longer annealing times [Barcellini, C., Dumbill, S., Jimenez-Melero E. (2018)]. At this annealing temperature, larger Nb(C,N) particles become enriched in Si and Ni at the phase boundaries, hinting towards a transition to G-phase [Barcellini, C., Dumbill, S., Jimenez-Melero E. (2018)]. The increase in annealing temperature above 950°C causes a reduction in the volume fraction of Nb(C,N) particles, together with an increase in the average particle size. As a consequence of the dissolution of the smaller particles, the austenite grain size increases and the material hardness reduces gradually. According to the model, abnormal grain growth is expected to occur for $0.25 \leq Z \leq 1$, see Fig. 4b.

The minimum $R/\bar{R}$ value for abnormal grain growth increases with the Z value up to Z~1. The data point for 1000°C in Fig. 4b lies just on the $(R/\bar{R})min$ curve, whereas Z decreases to 0.42 at 1100°C and approaches the region where normal & abnormal grain growth are predicted to occur. At the latter temperature, we have observed a significant grain growth in the austenite matrix, but we have not detected any austenite grain whose sizes is at least five times larger than the average grain size, so as to be classified as abnormal grain growth [Humphreys, F.J. (1997b)]. The approach of annealing 20Cr-25Ni Nb-stabilized stainless steel at 930°C therefore ensures the maximum fraction of HAGB and CSL boundaries, esp. twin boundaries, a refined austenite grain size and the maximum volume fraction of fine Nb(C,N) particles dispersed in the austenite matrix, and therefore provides the cladding material with enhanced resistance to water corrosion and thermal creep.

5. Conclusions

We have performed an in-depth characterization of the microstructure evolution of 20Cr-25Ni Nb-stabilized austenitic stainless steel during 1h isochronal annealing using scanning electron microscopy. The initial deformed microstructure undergoes recrystallisation via a strain-induced boundary migration mechanism, attaining a fully recrystallised microstructure at 850°C. Prior to the start of recrystallisation, a number of twins are formed close to the deformation bands present in the plastically deformed microstructure. A further increase in the annealing temperature does not modify significantly the austenite matrix until 950°C is reached. However, the volume fraction of Nb(C,N) particles increases during recrystallisation and attains a maximum at 930°C. At higher annealing temperatures, the smaller particles are thermally unstable and dissolve in the matrix. This particle dissolution gradually releases the Zener pinning pressure on the austenite grain boundaries, and consequently triggers the grain growth in the matrix of the material. The evolution of the microstructure upon 1h isothermal annealing up to 1100°C can be predicted using a unified model of cellular microstructures, based on the migration of high and low angle grain boundaries.

Acknowledgments

We acknowledge the Engineering and Physical Sciences Research Council (EPRSC) (EP/L014041/1) for providing funding for this project. We would also like to thank Dr. S. Walters from the National Nuclear Laboratory for providing the starting material.

References

1. Al-Shater, A., Engelberg, D., Lyon, S., Donohoe, C.,Walters, S., Whillock, G., Sherry, A. (2017), Characterization of the stress corrosion cracking behavior of thermally sensitized 20Cr-25Ni stainless steel in a simulated cooling pond environment, *J. Nucl. Sci. Technol.* 54, 742–751.

2. Andersen, I., Grong, Ø., Ryum, N. (1995a), Analytical modelling of grain growth in metals andalloys in the presence of growing and dissolving precipitates—I. Normal grain growth, *Acta Metall. Mater.*43, 2673–2688.

3. Andersen, I., Grong, Ø., Ryum, N. (1995b), Analytical modelling of grain growth in metals andalloys in the presence of growing and dissolving precipitates—II. Abnormal grain growth, *Acta Metall. Mater.* 43, 2689–2700.

4. Anderson, M. P., Srolovitz, D. J., Grest, G. S., Sahni, P.S. (1984), Computer simulation of

grain growth-I. Kinetics, *Acta Metall.* 32, 783–791.

5. Ardell, A. J. , Bellon, P. (2016), Radiation-induced solute segregation in metallic alloys, *Curr.Opin. Solid State Mater. Sci.* 20, 115–139.

6. Avrami, M. (1939), Kinetics of Phase Change. I. General Theory, *J. Phys. Chem.* 7, 1103-1112.

7. Avrami, M. (1940), Kinetics of Phase Change. II. Transformation-Time Relations for Random Distribution of Nuclei, *J. Phys. Chem.* 8, 212-224.

8. Avrami, M. (1941), Kinetics of Phase Change. III. Granulation, Phase Change, and Microstructure, *J. Phys. Chem.* 9, 177-184.

9. Bachmann, F., Hielscher, R., Schaeben, H. (2010), Texture Analysis with MTEX -- Free and Open Source Software Toolbox, in Texture and Anisotropy of Polycrystals III, vol. 160, pp. 63–68.

10. Barcellini, C., Dumbill, S., Jimenez-Melero E. (2018), Isothermal annelaing behaviour of nuclear grade 20Cr-25Ni austenitic steel, *Mater. Charact.* 145, 303-311.

11. Brandon, D. G. (1996), The structure of high-angle grain boundaries, *Acta Metall.* 14, 1479–1484.

12. Bunge, H.-J. (1982), *Texture analysis in materials science: mathematical methods*. Butterworths.

13. Burke, D. T. J. (1952), Recrystallization and grain growth, *Prog. Met. Phys.* 2, 220–292.

14. Carpenter, H. C. H., Tamura, S. (1962), The formation of twinned metallic crystals, Proc. Roy. Soc. (London) 113A, 161-182.

15. Chen, A. Y., Hu, W. F. , Wang, D., Zhu, Y. K., Wang, P., Yang, J. H., Wang, X. Y., Gu,

16. J. F., Lu, J. (2017), Improving the intergranular corrosion resistance of austenitic stainless

steel by high density twinned structure, *Scripta Mater.* 130, 264–268.

17. Fanfoni, M., Tomellini, M. (1998), The Johnson-Mehl-Avrami-Kolmogorov model: A brief review, *Nuovo Cim. D* 20, 1171–1182.

18. Fridman, E. M., Kopetskji, C. V., Shvindlermann, L. S. (1975), Effects of orientation and concentration factors on migration of individual grain boundaries in aluminum, *Z. Metallk.* 66, 533-539.

19. Fullman, R. L., Fisher, J.C. (1951), Formation of Annealing Twins During Grain Growth, J. Appl. Phys. 22, 1350- 1355.

20. Gottstein, G., Shvindlerman, L. S. (1992), On the orientation dependence of grain boundary migration, *Scripta Metall. Mater.* 27, 1515–1520.

21. Huang, Y., Humphreys, F. J. (2000), Subgrain growth and low angle boundary mobility in aluminium crystals of orientation $\{110\}\langle 001\rangle$, *Acta Mater.* 48, 2017–2030.

22. Humphreys, F. J. (1977), The nucleation of recrystallization at second phase particles in deformed aluminium, Acta Metall. 25, 1323–1344.

23. Humphreys, F.J. (1979), Recrystallization mechanisms in two-phase alloys, *Met. Sci.* 13, 136–145.

24. Humphreys, F. J. (1997a), A unified theory of recovery, recrystallization and grain growth, based on the stability and growth of cellular microstructures---I. The basic model, *Acta Mater.* 45 4231–4240.

25. Humphreys, F.J. (1997b), A unified theory of recovery, recrystallization and grain growth, based on the stability and growth of cellular microstructures---II. The effect of second-phase particles, *Acta Mater.* 45, 5031–5039.

26. Humphreys, F. J. (1999), Quantitative metallography by electron backscattered

diffraction, *J.Microsc.* 195,170–185.

27. Humphreys, F. J. (2001), Review Grain and subgrain characterisation by electron backscatter diffraction, *J. Mater. Sci.* 36, 3833–3854.

28. Humphreys, F. J., Hatherly, M. (2012), *Recrystallization and Related Annealing Phenomena*. Elsevier Science.

29. Jazaeri, H., Humphreys, F. J. (2004), Quantifying recrystallization by electron backscatter diffraction, *J. Microsc.* 213, 241–246.

30. Jones, A. R., Howell, P. R., Ralph, B. (1977), *Changes in grain boundary structure during the initial stages of recrystallization*, Phil. Mag. 35, 603-611.

31. Jones, A. R., Ralph, B. (1975), The influence of recrustallization on carbide particle distributions in a fully stabilized austenitic steel, *Acta Metall.* 23, 355-362.

32. Johnson, W. A., Mehl, R. F. (1939), *R*eaction Kinetics in Processes of Nucleation and Growth, *Trans. Am. Inst. Min. Metall. Eng*. 135, 16-442.

33. Kenik, E. A., Inazumi, T., Bell, G. E. C. (1991), *Radiation-induced grain boundary segregation and sensitization of neutron-irradiated austenitic stainless steel*, J. Nucl. Mater. 183, 145-153.

34. Kolmogorov, A. N. (1937), On the Statistical Theory of Crystallization of Metals, *Izv. Akad. Nauk SSSR, Ser. Mat.*, No. 3, 355-359.

34

5. Knowles, G. (1977), The Creep Strength of 20%Cr-25%Ni-Nb Steel Containing Controlled Particle Dispersions, *Met. Sci.* 11, 117–122.

36. Kronberg, M. L., Wilson, F. H. (1949), Secondary recrystallization in copper, *Trans, AIME* 185, 501.

37. Lobb, R. C., Evans, H. E. (1984), A determination of the chromium concentration for "healing" layer formation during the oxidation of chromium depleted 10Cr-25Ni-Nb stainless steel, *Corros. Sci*. 24, 385-396.

38. Nes, E. (1995), Recovery revisited, *Acta Metall. Mater.* 43, 2189–2207.

39. Nes, E., Ryum, N., Hunderi, O. (1985), On the Zener drag, *Acta Metall.* 33,11–22.

40. Powell, D. J., Pilkington, R., Miller, D. A. (1985), Influence of thermal ageing on creep properties of 20/25/nb stabilezed steel, *Institute of Metals books*, Stainless Steel 84, vol. 320, 382-390.

41. Powell, D. J., Pilkington, R., Miller, D. A. (1988), The precipitation characteristics of 20%Cr/25%Ni – Nb stabilised stainless steel, *Acta Metall.* 36, 713-724.

42. Ramaswamy, V., West, D. R. F (1970), NbC Precipitation in 20%Cr-25%Ni-1%Nb Austenitic Steel, *J. Iron Steel Inst.* 208, 391–394.

43. Randle, V., Brown, A. (1989), Development of grain misorientation texture, in terms of coincident site lattice structures, as a function of thermomechanical treatments, *Phil. Mag. A* 59(5), 1075-1089.

44. Read, W. T., Shockley, W. (1950), Dislocation Models of Crystal Grain Boundaries, *Phys. Rev*. 78, 275–289.

45. Rohrer, G. S. (2011), Grain boundary energy anisotropy: a review, *J. Mater. Sci.* 46, 5881–5895

46. Rollett, A. D., Srolovitz, D. J., Anderson, M. P. (1989), Simulation and theory of abnormal grain growth---anisotropic grain boundary energies and mobilities, *Acta Metall.* 37, 1227–1240.

47. Roussel, L. Y., Stokes, D. J., Gestmann, I., Darus, M., Young, R. J. (2009), Extreme high resolution scanning electron microscopy (XHR SEM) and beyond, *Conf. Proc. SPIE* 7378,

Scanning Microscopy.

48. Smith, C. S. (1952), Grain shapes and other metallurgical applications of topology, *Met. Interfaces, ASM, Cleveland, OH*, pp. 65–108.

49. Smith. C. S. (1948), Grains, Phases, and Interfaces, *Trans. Met. Soc. A.I.M.E.*, 175, pp. 15–51.

50. Sourmail, T. (2001), Precipitation in creep resistant austenitic stainless steel, *Mater. Sci. Technol.* 17 (2001) 1-14.

51. Sutton, A. P., Balluffi. R. W. (1996), *Interfaces in crystalline materials*, Clarendon.

52. Taylor, C. (1986), The Formation of Sensitised Microstructures during the Irradiation of CAGR Fuel Pin Cladding, in *Radiation-induced Sensitisation of Stainless Steel*.

53. Thompson, C. V., Frost, H. J., Spaepen, F. (1987), The relative rates of secondary and normal grain growth, *Acta Metall.* 35, 887–890.

54. Vandermeer, R. A. (1995), D.J. Jensen, Quantifying recrystallization nucleation and growth kinetics of cold-worked copper by microstructural analysis, *Metall. Mater. Trans. A* 26 (1995) 2227–2235.

55. Vujic, S., Sandstrom, R., Sommitsch, C. (2015), Precipitation evolution and creep strength modelling of 20Cr25NiNbN austenitic steel, *Mater. High Temp.* 32, 607-618.

56. Was., G. (2007) *Fundamentals of Radiation Materials Science*. Springer-Verlag.

57. Whillock, G. O. H., Hands, B. J., Majchrowski, T. P., Hambley, D. I. (2018), Investigation of thermally sensitised stainless steels as analogues for spent AGR fuel cladding to test a corrosion inhibitor for intergranular stress corrosion cracking, *J. Nucl. Mater.* 498, 187-198.

58. Young, R., Henstra, S., Chmelik, J., Dingle, T., Mangnus, A., Van Veen, G., Gestmann, I. (2009), XHR SEM: enabling extreme high resolution scanning electron microscopy, *Conf. Proc. SPIE 7378*, Scanning Microscopy.

Figure

Fig. 1. BSE micrographs of 20Cr-25Ni Nb-stabilised stainless steel after 1h of annealing at selected temperatures. 'As Rec.' denotes the as-received microstructure as a reference prior to annealing.

Fig. 2. (a) Inverse pole figure colour map (b) grain boundary misorientation map of the same region of interest in the microstructure, together with (c) BSE images of the microstructure at selected annealing temperatures.

Fig. 3. Temperature dependence of (a) Vickers hardness and average austenite grain diameter, (b) grain boundary length fraction, and (c) mean Nb(C, N) particle diameter and volume fraction. 'LAGB' and 'HAGB' denotes low-angle and high-angle grain boundaries, whereas 'CSL' stands for special coincidence site lattice boundaries, see Section 2. The background colour highlights the transition with increasing annealing temperature from deformed microstructure (blue) to a regime where recrystallization (green) and grain growth (light red) occurs.

Fig. 4. Solution of Eq. 4 for (a) recovery and recrystallization assuming $R=2.5\bar{R}$ (black lines) and $R=\infty$ (blue line), and for (b) grain growth, see text.

Fig. 5. Kernel average misorientation map showing an example of strain induced boundary migration in the microstructure after annealing at 800ºC for 1h. HAGBs and CSL boundaries are coloured in black, whereas LAGBs are displayed in magenta.

Fig 6. BSE micrographs showing the distribution of Nb(C, N) particles in the microstructure after 1h annealing heat treatment at 930ºC. LAGBs are coloured in black, HAGBs in blue, CSL Σ3 in red, CSL Σ9 in cyan and CSL Σ11 in magenta respectively.

Additional Figure. TEM BF micrograph showing the microstructure of (a) the as received condition, and also after annealing for 1h at (b) 400ºC and (c) 930 ºC.

Lay Description:

Austenitic stainless steel containing high percentage of chromium and nickel is currently used as fuel cladding material in the British Advanced Gas-cooled Reactors (AGR). This material has been chosen because of its high resistance to thermal creep and corrosion, both enhanced by the presence of a fine dispersion of carbo-nitrides precipitated during the cladding thermomechanical processing. During the time spent in the reactor core, few fuel cladding elements can become susceptible to local chromium depletion at grain boundaries, which is ascribed to the time evolution of the microstructural damage caused by the neutron bombardment in the reactor core. This depletion might increase the susceptibility of this steel to intergranular corrosion attacks during medium-to-long term storage of spent fuel elements in water ponds. The severity of the local chromium depletion depends not only on the irradiation conditions, but also on the grain boundary geometry. We have investigated the recovery, recrystallisation and grain growth of AGR stainless steel during 1h annealing at selected temperatures relevant for the thermomechanical processing of the steel claddings, focusing on the formation and evolution of grain boundaries and second phases. These two features play a key role in the progression of the neutron damage and the subsequent development of local chromium depletion during reactor service operations. A deep understanding of the mechanisms and conditions behind their formation during the thermomechanical processing of the cladding material and their interaction with each other constitutes the foundation to evaluate, and potentially mitigate, the effect of irradiation on the cladding material.

Table 1. Chemical composition (wt.%) of the Nb-stabilised austenitic steel used in this study.

C	Mn	Si	S	P	Cu	Ni	Cr	Mo	Nb	V	Al	Ti	N	Fe
0.058	0.59	0.58	0.002	<0.003	<0.01	23.98	19.12	<0.01	0.57	<0.01	0.017	0.01	0.009	Bal.

Table 2. Microstructural parameters relevant for the description of the annealing behaviour of 20Cr 25Ni Nb-stabilised stainless steel. The austenite matrix is characterised by the average grain (*D*) and subgrain (D_{sub}) diameter, together with the average grain ($\overline{\theta}$) and subgrain ($\overline{\theta_{sub}}$) misorientation angle. The Nb(C,N) particle distribution is defined by its average grain diameter (*d*), volume fraction (f_v) and Z parameter. 'As Rec.' denotes the as-received microstructure.

T (°C)	D(μm)	D_{sub}(μm)	$\overline{\theta}$ (°)	$\overline{\theta_{sub}}$(°)	d(nm)	f_v(%)	Z
As Rec.	7.5	1.2	14.6	5.3	161	0.64	0.072*
400	16.3	3.7	23.6	4.4	131	0.04	0.016*
600	13.2	1.9	22.8	4.5	140	0.18	0.035*
700	8.9	2.7	29.0	5.0	94	0.77	0.331*
800	4.0	3.4	48.5	6.4	103	1.39	0.691*
930	4.4	-	48.5	-	95	2.66	1.839**
1000	20.2	-	-	-	125	0.32	0.780**
1100	47.1	-	45.5	-	156	0.09	0.421**

Calculated using (*) the subgrain diameter or (**) the grain diameter.

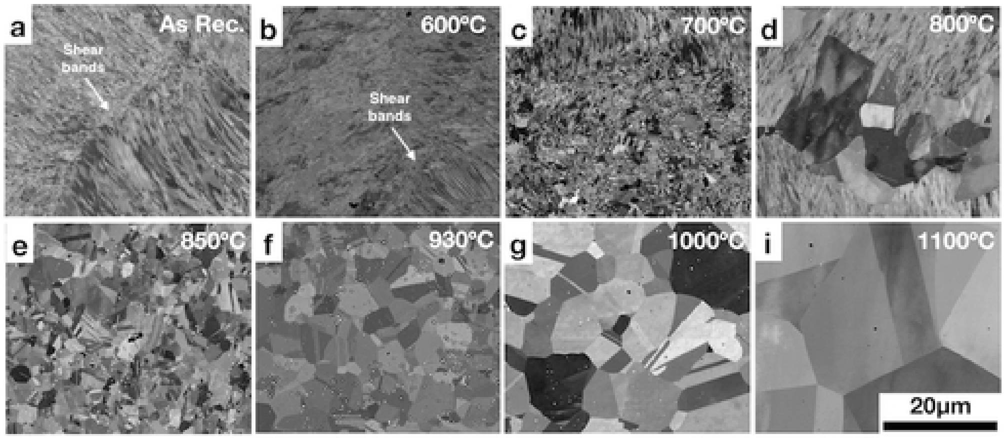

Fig. 1. BSE micrographs of 20Cr-25Ni Nb-stabilised stainless steel after 1h of annealing at selected temperatures. 'As Rec.' denotes the as-received microstructure as a reference prior to annealing.

43x18mm (300 x 300 DPI)

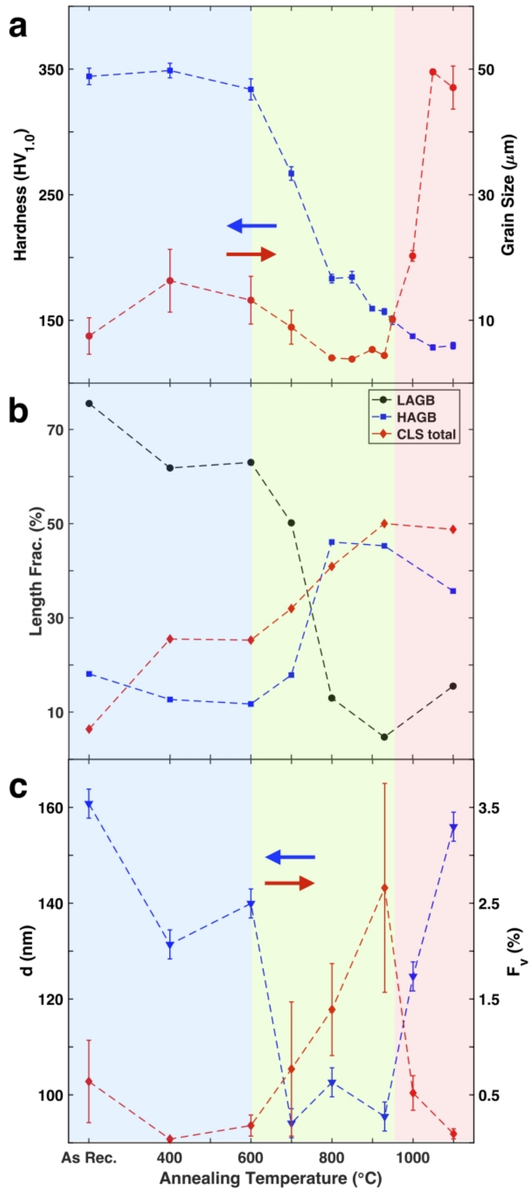

Fig. 3. Temperature dependence of (a) Vickers hardness and average austenite grain diameter, (b) grain boundary length fraction, and (c) mean Nb(C, N) particle diameter and volume fraction. 'LAGB' and 'HAGB' denotes low-angle and high-angle grain boundaries, whereas 'CSL' stands for special coincidence site lattice boundaries, see Section 2. The background colour highlights the transition with increasing annealing temperature from deformed microstructure (blue) to a regime where recrystallization (green) and grain growth (light red) occurs.

159x357mm (300 x 300 DPI)

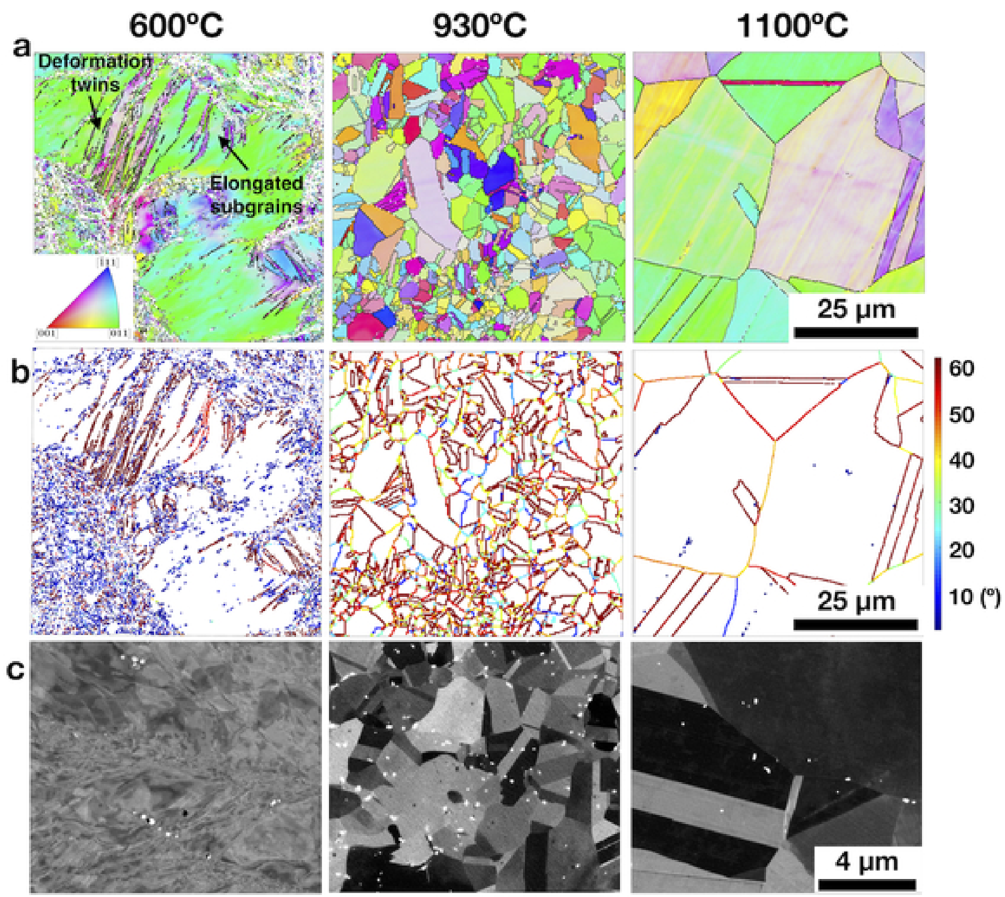

Fig. 2. (a) Inverse pole figure colour map (b) grain boundary misorientation map of the same region of interest in the microstructure, together with (c) BSE images of the microstructure at selected annealing temperatures.

48x43mm (300 x 300 DPI)

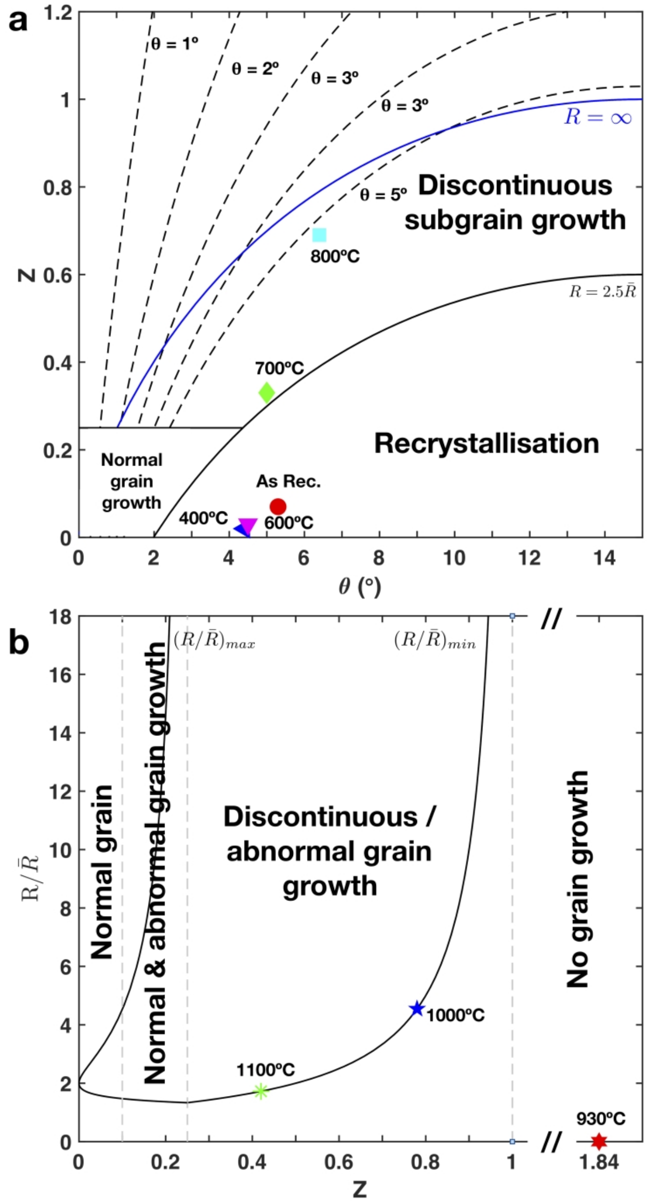

Fig. 4. Solution of Eq. 4 for (a) recovery and recrystallization assuming R=2.5R (black lines) and R=∞ (blue line), and for (b) grain growth, see text.

192x356mm (300 x 300 DPI)

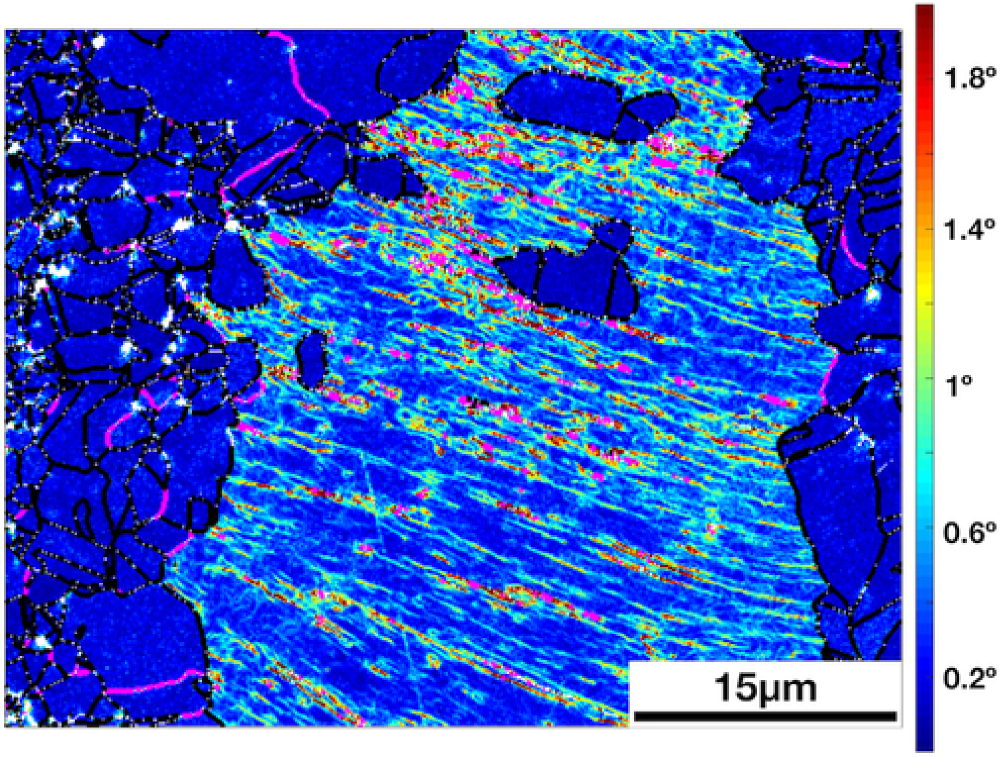

Fig. 5. Kernel average misorientation map showing an example of strain induced boundary migration in the microstructure after annealing at 800ºC for 1h. HAGBs and CSL boundaries are coloured in black, whereas LAGBs are displayed in magenta.

42x32mm (300 x 300 DPI)

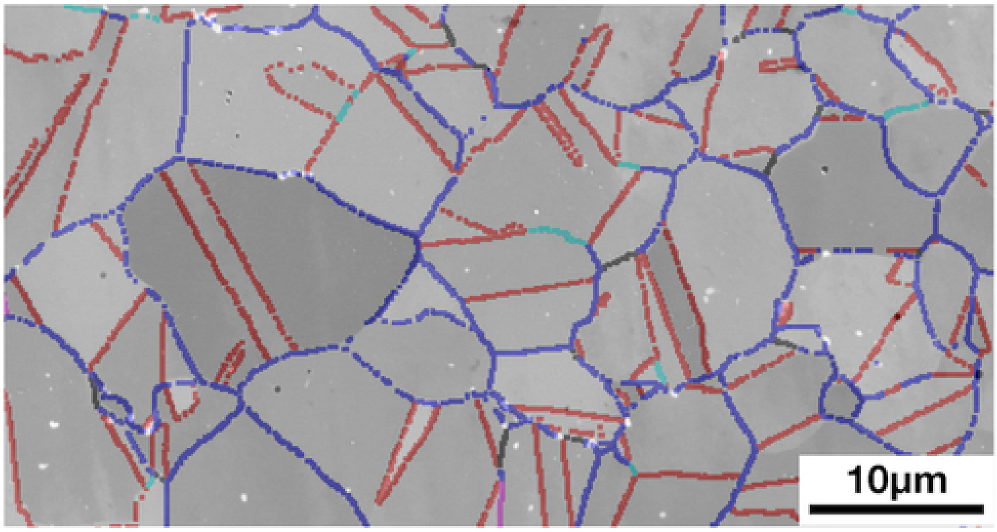

Fig 6. BSE micrographs showing the distribution of Nb(C, N) particles in the microstructure after 1h annealing heat treatment at 930ºC. LAGBs are coloured in black, HAGBs in blue, CSL Σ3 in red, CSL Σ9 in cyan and CSL Σ11 in magenta respectively.

43x23mm (300 x 300 DPI)

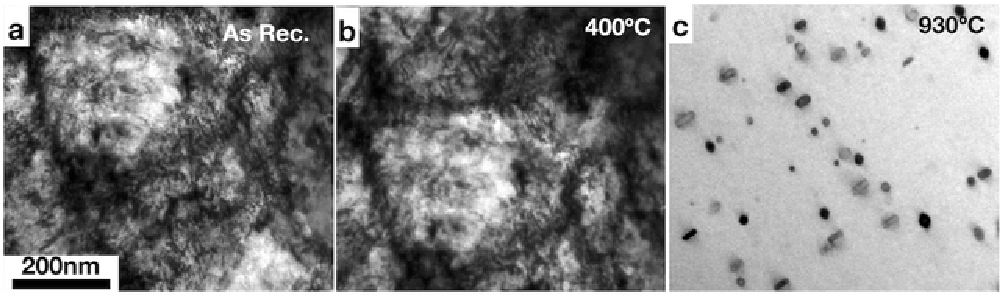

Additional material

54x15mm (300 x 300 DPI)